Physics of Plasmas

Target normal sheath acceleration with a large laser focal diameter

Cite as: Phys. Plasmas **27**, 123104 (2020); https://doi.org/10.1063/5.0020609
Submitted: 02 July 2020 . Accepted: 25 November 2020 . Published Online: 21 December 2020

J. Park, J. H. Bin, S. Steinke, et al.

Physics of Plasmas ARTICLE scitation.org/journal/php

Target normal sheath acceleration with a large laser focal diameter

Cite as: Phys. Plasmas **27**, 123104 (2020); doi: 10.1063/5.0020609
Submitted: 2 July 2020 · Accepted: 25 November 2020 ·
Published Online: 21 December 2020

J. Park, J. H. Bin, S. Steinke, Q. Ji, S. S. Bulanov,[a] M. Thévenet, J.-L. Vay, T. Schenkel, C. G. R. Geddes, C. B. Schroeder, and E. Esarey

AFFILIATIONS

Lawrence Berkeley National Laboratory, Berkeley, California 94720, USA

[a]Author to whom correspondence should be addressed: sbulanov@lbl.gov

ABSTRACT

The dependence of the laser-driven ion acceleration from thin titanium foils in the Target Normal Sheath Acceleration (TNSA) regime on target and laser parameters is explored using two dimensional particle-in-cell simulations. The oblique incidence ($\theta_L = 45°$) and large focal spot size ($w_0 = 40\mu$m) are chosen to take an advantage of quasi one-dimensional geometry of sheath fields and effective electron heating. This interaction setup also reveals low and achromatic angular divergence of a proton beam. It is shown that the hot electron temperature deviates from the ponderomotive scaling for short laser pulses and small pre-plasmas. This deviation is mainly due to the laser sweeping, as the short duration laser pulse each moment in time effectively heats only a fraction of a focal spot on the foil. This instantaneous partial heating results in an electron temperature deviation from the ponderomotive scaling and, thus, lower maximum proton energies than it could have been expected from the TNSA theory.

I. INTRODUCTION

Plasma-based particle acceleration has been extensively studied for several decades driven by the rapid development of high power lasers. Laser-based ion acceleration has attracted considerable attention for the potential applications to many scientific research areas and industries: fundamental particle physics, inertial confinement fusion, warm-dense matter, medical therapy, isochoric heating of solid matter, etc. (see reviews in Refs. 1–5 and references cited therein for the discussion on recent studies and applications). It is understood that laser ion acceleration behaves quite differently depending on the parameters of the laser and the target, allowing the identification of several distinct mechanisms of acceleration:[6] Target Normal Sheath Acceleration (TNSA),[7–10] Radiation Pressure Acceleration (RPA),[11–13] Shock Wave Acceleration (SWA),[14] Relativistic Transparency (RIT),[15] and Magnetic Vortex Acceleration (MVA).[16,17] Among them, TNSA has been known as the most stable and well-studied ion acceleration scheme (see, e.g., Ref. 18 for the current record accelerated proton energy using TNSA).

In TNSA, an intense laser light irradiates a few micro-meter thickness solid target and populates tenuous hot electrons. The electron temperature can reach up to $T \sim$ MeV possibly via the resonant[19] and/or non-resonant[20,21] interaction. The hot electrons leaving the target surface induce a strong sheath electric field of the order of TV/m along the normal direction at the front/rear-surfaces, and the ions from the main target and/or contaminant layers are accelerated. The maximum ion energy of TNSA scales with the laser intensity as $\propto I^{0.5-1.0}$,[22] and most TNSA studies have focused on a small focal diameter of the laser beam with a few micrometers[23] in order to increase the electron temperature $T_e \propto I^{1/2}$ and the ion energy as a result of the hot electrons. However, the number of ions at the high-energy end of the spectrum can be as low as $10^7 - 10^8$ particles[24] and the angular divergence is large, in general. In order to address these issues in the framework of TNSA without involving other mechanisms that would require high intensity, or ultra-thin targets, or both, it is interesting to consider a different interaction setup. In particular, if the generation of high energy ions is not required.

We propose to study a large focal spot laser pulse interaction with μm-scale foils in the TNSA regime using two-dimensional particle-in-cell (2D PIC) simulations. The oblique incidence ($\theta_L = 45°$) and large focal spot size ($w_0 = 40\mu$m) were chosen to take an advantage of quasi one-dimensional geometry and effective electron heating as well as to resemble a typical experimental setup. It is well known that the pre-plasma scale length plays an important role in laser-driven ion acceleration, see Refs. 25–35. In Ref. 36, this was used to determine the pre-plasma scale length by comparing the results of PIC simulations and experimental data. This analysis revealed the

departure of the maximum ion energy values from the TNSA theory prediction. In this paper, we point out that the sweeping effect is very sensitive to the actual pre-plasma scale length.

Whereas long pulses reproduce ponderomotive scaling well, in the case of short pulses and small pre-plasma scale-lengths the deviation from this scaling is quite significant. It is partially connected with less efficient electron heating and the "sweeping" effect.[36] The latter corresponds to the fact that large focal spot diameter laser pulses with $\tau < \omega_0/c$ irradiate only a fraction of the focal region on the foil at a given moment in time. This irradiated region "sweeps" across the focal region, providing only local heating of the electron population over a period of time that establish sheath fields at the back of the target, which are smaller than it could have been expected from the TNSA theory.[5]

In addition to the study of the deviation from the ponderomotive scaling, we show that for a large focal spot diameter, the proton beam quality is improved compared to the small spot case: (i) the angular divergence is about 100 mrad and is highly achromatic and (ii) the number of accelerated protons is increased up to $\sim 10^{11}$ with the energy above 5 MeV, which is mainly due to the geometry of the interaction. Such proton beam parameters might be advantageous for a number of applications.

This paper is organized as follows: the simulation setup and the parameter space are described in Sec. II. The simulation results are presented in Sec. III. The summary and conclusion are given in Sec. IV.

II. PIC SIMULATION SETUP

We use the relativistic particle-in-cell (PIC) code Warp, developed at LBNL, for this study.[37,38] The simulations used only PIC modules without additional collision module. Hence, only the long range collisions covered by the resolution of the simulation grid that supports electromagnetic fields were covered. The particles current was deposited on the simulation grid using third-order (cubic) particle shape, mitigating numerical heating.[39] A study was performed by running a sample simulation with increasing resolution to confirm convergence and exclude the presence of the numerical artifacts.

As illustrated in Fig. 1, the simulation domain is 2D with the sizes $(L_z, L_x) = (147\mu\text{m}, 357\mu\text{m})$. The main target is titanium ions Ti^{11+} and electrons, located at $z_0 = 96\mu$m with one micrometer thickness ($z_{rear} = z_0 + 1\ \mu$m). Here and in what follows, we define the position of target front at z_0 and back at z_{rear}. The introduction of the exponential pre-formed plasma at the front and rear sides of the target (see below) does not allow for the clear definition of the target thickness, which is why we employ the one given above. The electron density of the target is $n_e = 300 n_{\text{crit}}$, where $n_{\text{cr}} = m_e\omega^2/(4\pi e^2)$ is the critical density, m_e is the electron mass, ω is the laser angular frequency, and e is the electron charge.

The laser transverse and longitudinal profiles are Gaussian. We simulate both normal and oblique incidence at the target (see Fig. 2). In the latter case, the angle between the laser propagation direction and the target normal direction is 45°. The laser wavelength is $\lambda = 0.8\mu$m. Here, we adopt a large focal diameter of $2w_0 = 100\lambda$ (w_0 is the laser waist). The center of the virtual laser antenna is located at $z = 40\mu$m to avoid an overlap with the main target. The temporal peak at the center of the laser pulse arrives at the target front surface at $t = 614$ fs. The laser is linearly polarized in the $x - z$ plane (p-pol). We vary the laser pulse duration from $\tau = 35$ fs to 300 fs. The duration is

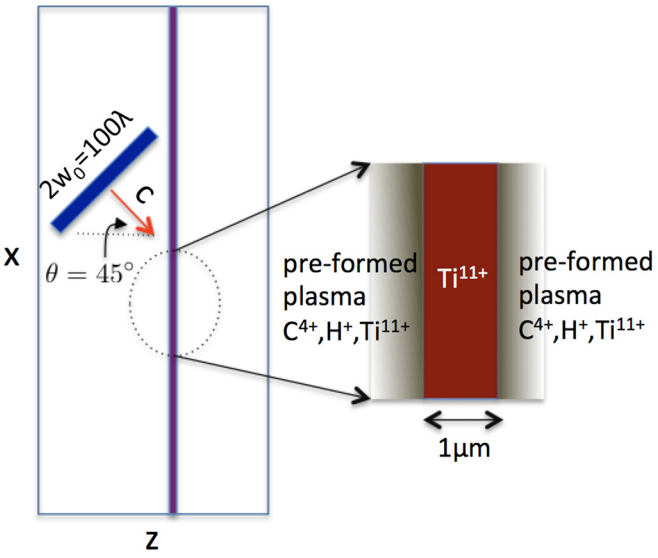

FIG. 1. 2D PIC simulation setup: (left) obliquely ($\theta_L = 45°$) incident laser beam toward a thin titanium target. (right) Detailed target composition with a preformed plasma at the front and rear sides of the target.

defined as a half-width at $1/e$ of the field amplitude (or $\tau_{\text{FWHM}} = \sqrt{2\ln 2}\tau = 41 - 353$ fs) while keeping the laser energy constant. This means that the laser peak intensity varies from $I = 2.8 \times 10^{18}\text{W/cm}^2$ to $24 \times 10^{18}\text{W/cm}^2$ ($a_0 = 1.13 - 3.3$). Here, $a_0 = 0.85[I(\text{W/cm}^2)\lambda^2(\mu\text{m}) \times 10^{18}]^{1/2}$ is the dimensionless amplitude of the laser electromagnetic field vector potential. In order to identify the effects coming from oblique incidence and large focal diameter, we also simulate normal incidence [see Fig. 2(d)], as it was mentioned above, and small focal diameter [$2w_0 = 6\lambda$, see Fig. 2(e)] cases. For a small focal diameter, we keep peak intensity the same as in the case of a large one.

To account for the effect of the laser pre-pulse, we initialized transversely homogeneous pre-formed plasmas with a certain scale length at the front of the target, $n_e = n_0 \exp[(z - z_0)/L]$ for $z < z_0 = 96\mu$m. Here, L is the gradient scale length, which was varied from $L = 0$ to 0.1λ. At the rear of the target, we also setup a pre-formed plasma with a fixed gradient scale length, $L = 0.01\lambda$. We choose to simulate different pre-formed plasma gradient scale-lengths to show that the sweeping effect is very sensitive to it. Whereas sweeping effect leads to the deviation of the proton acceleration scaling from the ponderomotive one, this deviation is only present for a certain range of pre-plasma scale lengths.

In principle, the exact form of the pre-formed plasma should depend on the properties of the laser pre-pulse, i.e., precise spatial and temporal profiles, which are usually unknown. This dependence can be revealed through hydro simulations (see, e.g., Refs. 33 and 40–43), which are also model dependent and will add their own uncertainties on top of those from the model of laser pre-pulses. That is why we concluded that initializing pre-plasma homogeneously along the target is a good approximation of the result of pre-pulse interaction with the target.

To initialize the surface contamination, we added contaminant species, protons (H^+), and carbon ions (C^{4+}) on both sides of the

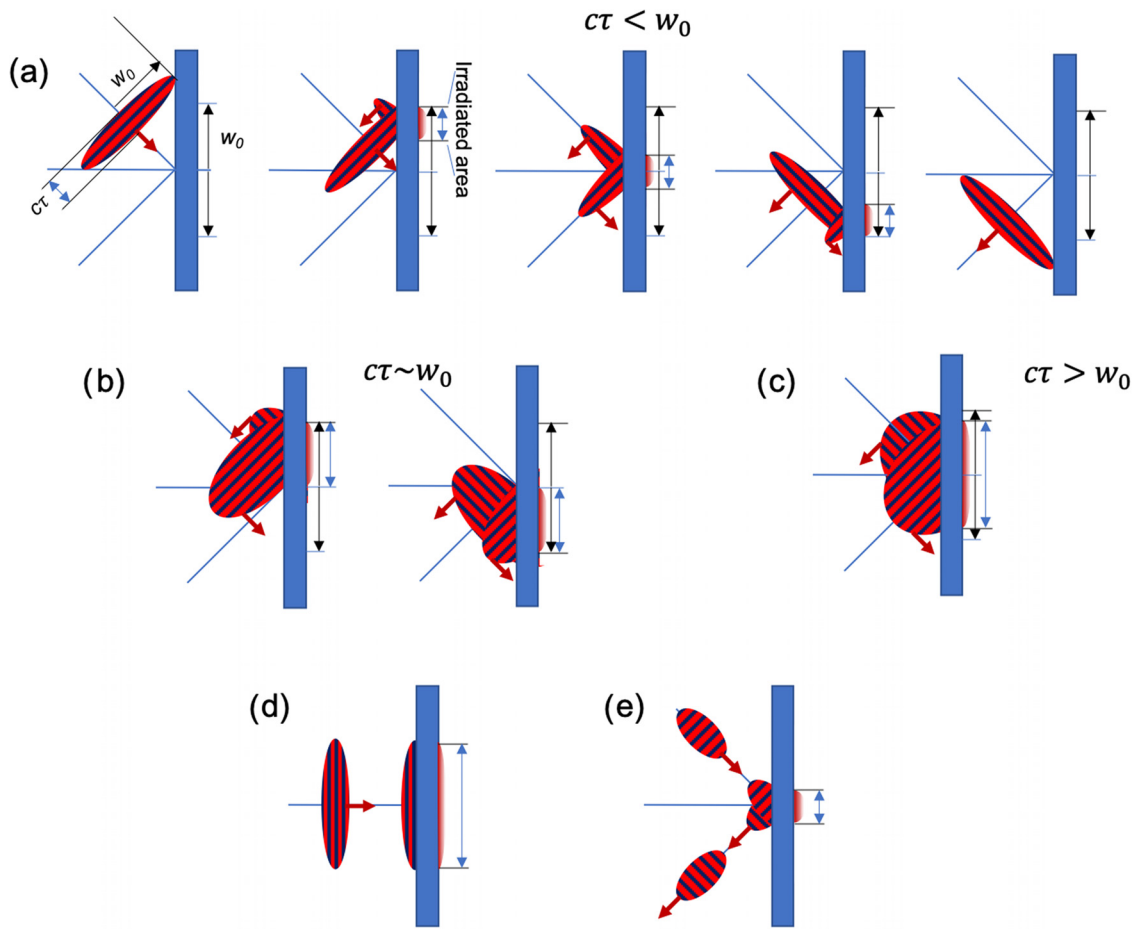

FIG. 2. The schemes of laser-target interaction simulated in the present paper: (a) the case of an obliquely incident laser pulse with a large focal diameter and short duration, $c\tau < w_0$, (b) the case of an obliquely incident laser pulse with a large focal diameter and intermediate duration, $c\tau \sim w_0$, (c) the case of an obliquely incident laser pulse with a large focal diameter and long duration, $c\tau > w_0$, (d) the case of a normally incident laser pulse with a large focal diameter, and (e) the case of an obliquely incident laser pulse with a small focal diameter.

target. The charge state $+4$ of the carbon ions is based on the probability of field ionization by the laser at the front of the target as well as by the sheath field at the back of the target.[44,45] The density profile of the contaminant layer is assumed to be the same exponential profile as the pre-formed plasma. The peak electron densities of the hydrogen and carbon ions are given by $50n_{\mathrm{crit}}$ and $100n_{\mathrm{crit}}$, respectively.

The number of cells is $(N_x, N_z) = (18\,432, 15\,120)$ and the cell sizes are $(dx, dz) = (0.02424\lambda, 0.01212\lambda)$. The boundary conditions are periodic along the transverse directions (x-axis) and open along the longitudinal direction (z-axis). From convergence tests, we used up to 320 particles per cell for protons (and corresponding electrons), 120 and 40 for titanium and carbon, respectively (1320 and 160 for corresponding electrons).

III. SIMULATION RESULTS

As it was mentioned in the introduction, the oblique incidence of a large focal diameter laser pulse at the target introduces a sweeping effect, which was identified in Ref. 36. When such a laser interacts with a foil, the effective spot on the target is defined as $c\tau w_0/\sqrt{w_0^2 + (c\tau)^2}$. If $c\tau \le w_0$, then the irradiated area sweeps across the $2w_0$ spot at the target [see Figs. 2(a) and 2(b)]. If $c\tau > w_0$, then the laser irradiates the whole $2w_0$ spot at the target for the most part of the interaction [see Fig. 2(c)].

This geometry of interaction has two important consequences. First, the dependence of the hot electron temperature on the duration of the laser pulse, which is varied from $c\tau \gg w_0$ to $c\tau \ll w_0$ with total laser energy being kept constant, demonstrates the deviation from the ponderomotive scaling. Second, the sweeping of the laser across the focal spot at the foil results in more efficient electron heating compared to not only a normal laser incidence case but also an oblique incidence of a small focal diameter laser with the same peak intensity.

For $c\tau \le w_0$, the simulations show that the hot electron temperature begins to decrease, whereas the ponderomotive scaling predicts an opposite trend. This is due to the fact that short pulses irradiate only a limited area of the foil at any given moment during the interaction. This irradiated area sweeps across the focal spot at the foil as the interaction evolves, resulting in a localized interaction and lower

absorption of the laser energy by the target. Long pulses, $c\tau \gg w_0$, irradiate the whole spot, which results in larger absorption, but the hot electron temperature is reduced due to lower laser intensity. Thus, at $c\tau \ll w_0$, hot electron temperature goes down because of localized interaction, and for $c\tau \gg w_0$, it goes down because of reduced laser intensity. This means that there exists an optimal laser duration, which maximizes hot electron temperature. In what follows, we look at the laser absorption and the resulting hot electron temperature in detail.

A. Electron temperature and proton acceleration

The results of 2D PIC simulations are presented in Fig. 3. The first two panels show the laser pulse absorption into the target, and the third one shows hot electron temperature as functions of laser pulse duration for different pre-plasma scale-lengths, $\theta = 45^\circ$, and $w_0 = 50\lambda$. The laser energy absorption is defined as $f = 100 \times (E_{in} - E_{ref})/E_{in}$, where E_{in} and E_{ref} are the energies of the initial and reflected laser pulses. The absorption increases with the pulse duration and saturates for $\tau > 150$ fs. In Fig. 3(b), the absorption is divided by the laser pulse duration for the comparison with hot electron temperature in Fig. 3(c), which matches rather good for a long pulse duration.

The hot electron temperature is measured at the rear side of the target and is averaged over $t_{peak} < t < t_{peak} + \tau$, where $t_{peak} = 614$ fs is the arrival time of the temporal and spatial peak of the laser pulse at the target front surface (a similar figure is found in Ref. 47, where the target thickness varies for a small focal size). The dashed line represents the ponderomotive temperature,[46] $T_e = (\gamma_t - 1)m_e c^2$, where $\gamma_t = (1 + I[\mathrm{W/cm^2}](\lambda[\mu\mathrm{m}])^2/1.37 \times 10^{18})^{1/2} \approx \sqrt{1 + a_0^2/2}$.

For a large density gradient scale length ($L = 0.1\lambda$), the electron temperature fits the ponderomotive scaling, indicating that the sweeping effect is totally mitigated by the expanding pre-plasma. However, for smaller scale-lengths, the deviation from the ponderomotive scaling becomes more pronounced, especially at a short laser pulse duration. Moreover, at $L = 0$ and $L = 0.01\lambda$, the temperature has a maximum at $\tau = 140$ fs and $\tau = 85$ fs, respectively. This is the effect of laser pulse sweeping. The optimal pulse duration to maximize the sweeping effect is obtained from a simple geometric matching condition, $\tau_{opt} \sim w_0/c \approx 133$ fs, which agrees with the simulation results. This matching condition is basically the situation when a significant portion of the focal spot at the foil is irradiated during the interaction.

We note that for $\tau \geq 150$ fs, the hot electron temperature is similar for different density gradient scale-lengths. This can be attributed to the fact that the leading edge of the laser pulse causes the pre-plasma to expand significantly before the intensity peak arrives at the target surface, modifying the density profile in a way that the difference between the initial density profiles is no longer seen.[47,48] As it was mentioned above, the sweeping effect is very sensitive to the actual density gradient scale length value. In Ref. 36, this effect was utilized to estimate the scale length by comparing the experimental data with the simulation results. It was found that $L = 0.01\lambda$ matches well the experimental data. Here, we also see that the sweeping effect is not observable for $L = 0.1\lambda$, is barely visible for $L = 0.05\lambda$, and is well pronounced for $L = 0.01\lambda$ and $L = 0$.

In what follows, we examine the mechanism of sweeping on proton acceleration time using the particle tracking method. In order to do so, we compare three cases: (i) $\theta_L = 45^\circ$, $w_0 = 50\lambda$; (ii) $\theta_L = 0$, $w_0 = 50\lambda$; and (iii) $\theta_L = 45^\circ$, $w_0 = 3\lambda$, where the peak intensity is the same as in (i) and (ii). The simulations are performed for $L = 0.01\lambda$. This comparison is needed to emphasize the difference of accelerating protons with a large focal spot laser pulse. First, we look at the difference between the normal and oblique incidences. It is well known that in TNSA obliquely incident laser pulse couples better to the target than normally incident ones. In order to compare the contribution of sweeping, we also simulate case (iii), where the advantages of oblique incidence are present, but the sweeping is not. The proton acceleration time is measured for those protons with the energy higher than 90% of maximum energy.

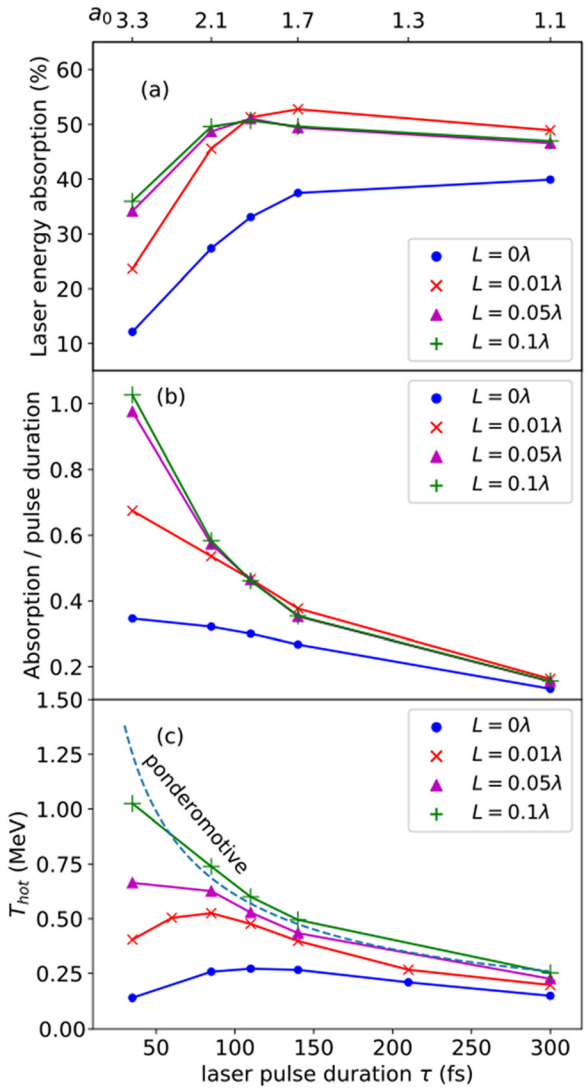

FIG. 3. Several variables as a function of pulse duration. Different colors represent different gradient scale lengths in the pre-plasma. The dimensionless vector potential a_0 is on the top-axis. The angle of laser incidence is $\theta_L = 45^\circ$ and the focal diameter is $2w_0 = 100\lambda$. (a) Laser energy absorption into the target; (b) laser energy absorption divided by the pulse duration; and (c) hot electron temperature (MeV). The ponderomotive temperature[46] is added for comparison (dashed line).

The inset in Fig. 4(a) illustrates an example of a field acting on a proton along its trajectory, $E_z = E_z(\mathbf{x}_p(t), t)$. The acceleration time, δt, is the full width of the curve at $1/e$ of the maximum value and is averaged over all high energy protons. For a short pulse duration, $\tau = 35$ fs, the acceleration times from all three cases are similar to each other. As the pulse duration becomes longer, the acceleration time from the sweeping case, (i), increases more than from other cases. However, at $\tau = 300$ fs, the acceleration times from (ii) and (iii) become similar, indicating overall reduction of acceleration efficiency and significant plasma density modification at the front surface of the target.

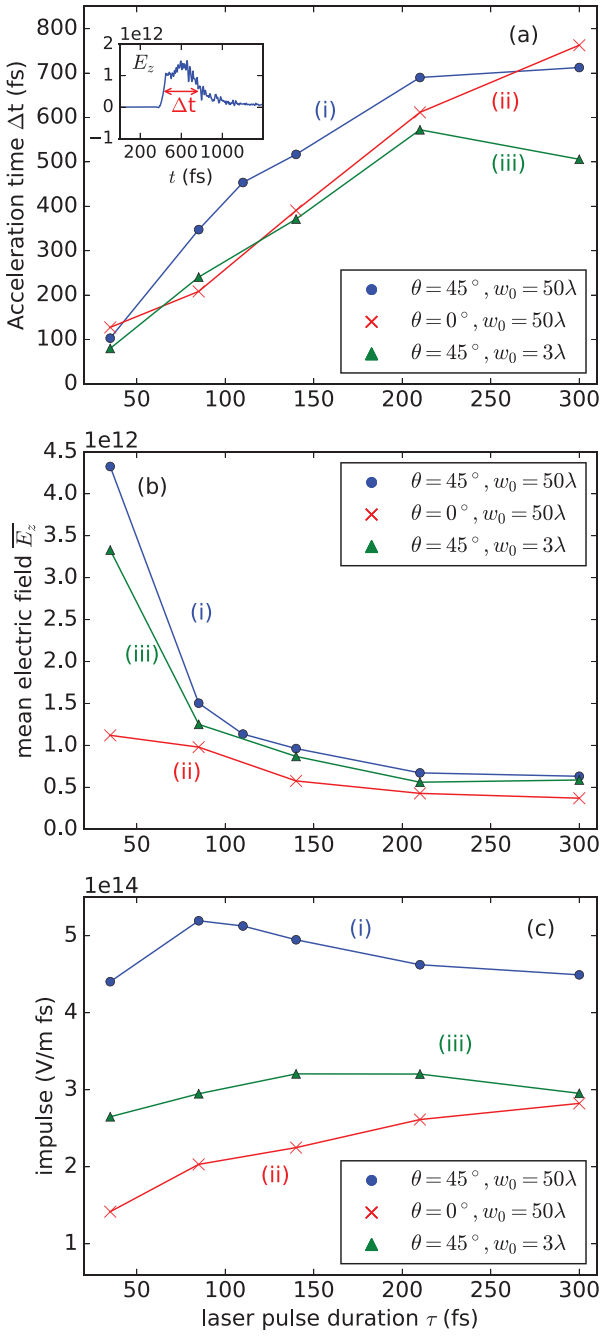

FIG. 4. Averaged quantities of energetic protons vs laser pulse duration for Runs II (blue), V (red), and IV (green) in Table I: (a) acceleration time, (b) electric field strength, and (c) momentum impulse. The inset in (a) is an example trajectory of the electric field $E_z(\mathbf{x}(t), t)$ acting on a single proton.

In Fig. 4(b), the mean electric field dependence on the laser pulse duration is shown. It is defined as $\delta t^{-1} \int E_z(t)dt$, averaged over all high energy protons. The electric field strength for the sweeping case (i) is only slightly higher than for (iii), which is due to the similar absorption level of laser energy to the target and originates from the oblique incidence in both cases. The normal incidence (iii) demonstrates the lower level of mean electric field strength due to lower laser energy absorption.

In order to see how the values of acceleration time and mean electric field combine into energy gain, we show the dependence of the mean momentum impulse, $\delta p = e \int E_z(t)dt$, averaged over the high energy protons, on the laser pulse duration. The sweeping case, (i), reveals higher momentum impulse than the other two. We note that the peak impulse is around $\tau = 85$ fs, when the electron temperature is maximized for $L = 0.01\lambda$ in Fig. 3(c).

Thus, we found that the electron temperature deviates from the ponderomotive scaling as the density gradient scale length becomes smaller, and the laser sweeping plays an important role by increasing the acceleration time of protons. The sweeping is optimized at a pulse duration of approximately $\tau \approx w_0/c$.

B. Proton beam profiles

In this subsection, the beam profile of the accelerated protons for a large focal diameter is examined. Figures 5(a) and 5(b) show a snapshot of the longitudinal electric field and the proton energy distribution during the acceleration stage at $t = 752$ fs in the $x - z$ space. In Fig. 5(a), the electric field vectors are directed almost along the normal axis at the rear surface, and the field structure reveals double layers due to the slowly moving carbon ions behind the protons. In Fig. 5(b), the energetic protons are located at the leading edge of the expanding proton plume, accelerated by the leading electric field [see the E_z field line-out at $x = 0$ (magenta line)], and are slightly tilted downward due to the obliquely propagating laser beam. Figure 5(c) shows the angular divergence of the proton beam as a function of the proton energy for different pulse durations (Run II). The divergence is defined by $2\Delta\theta = 2\sqrt{\langle\theta^2\rangle - \langle\theta\rangle^2}$; $\langle\rangle$ is an averaged quantity and $\theta = \sin^{-1}(p_x/p)$, where p_x and p are the x-component and the magnitude of the momentum, respectively. Here, the gradient scale length is fixed as 1% of the laser wavelength and we confirm that the divergence is insensitive to the gradient scale length (not shown in the figure). The divergence is exceptionally low, 50–100 mrad, compared to TNSA using a tight focus, and is achromatic almost from ~4 MeV up to the cutoff energy. Such a low and achromatic divergence is attributed to the large focal diameter and subsequent low transverse variability of the sheath fields and was also reported in the recent experiment (see Ref. 36 for details), where the divergence is a bit higher around $2\Delta\theta \approx 150$ mrad possibly due to 3D effects.

The 3D effects that are not captured by our 2D PIC simulations are mainly connected with the simulation geometry. Apart from

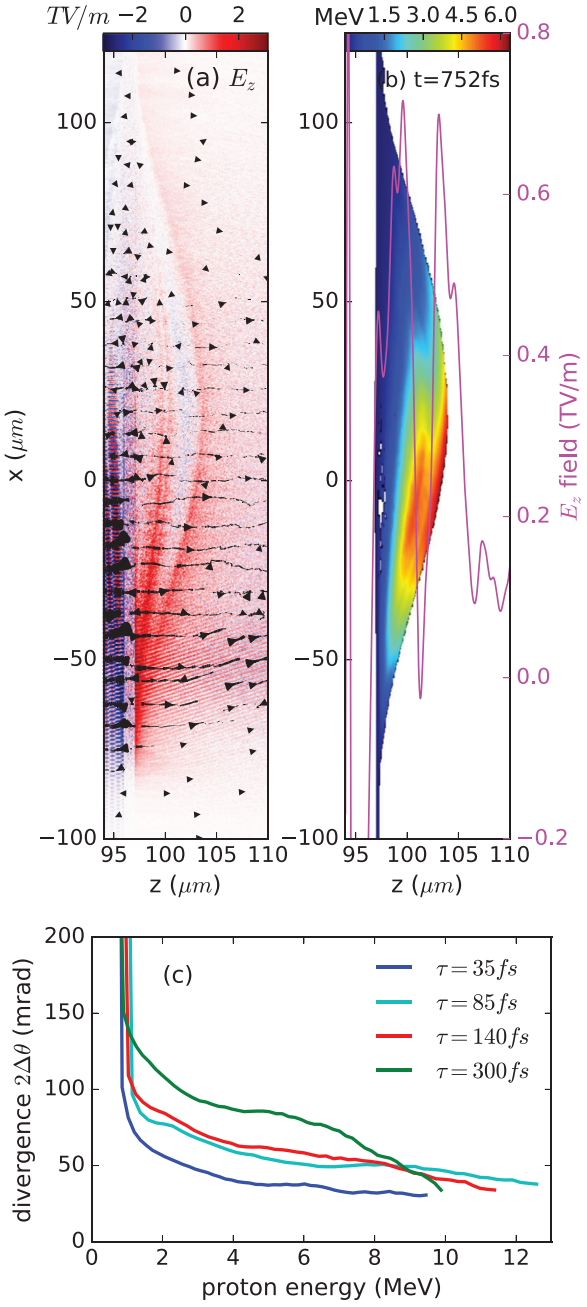

FIG. 5. (a) Electric field (E_z) and the field vector during the acceleration stage $t = 752$ fs in the $x - z$ space. (b) Proton energy distribution with the E_z field line-out at $x = 0$ (magenta). (c) Proton angular divergence as a function of the energy (Run II).

obvious laser polarization effects, the oblique incidence of the large focal diameter laser pulse leads to a significant difference between (x, z) and (y, z) planes. In Fig. 6, we show the schematics of the interaction in the (x, y) plane, i.e., how the irradiated spot would look at the foil. The spot is asymmetric with y-dimension determined by w_0 and x-dimension by $c\tau w_0/\sqrt{w_0^2 + (c\tau)^2}$, as it was mentioned above.

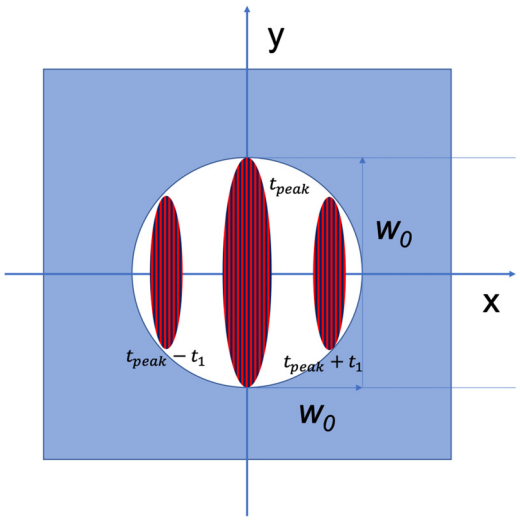

FIG. 6. The sweeping of the large focal diameter and short duration laser pulse across the focal spot at the foil.

Whereas such geometry does not make the field of the laser and the sheath field significantly differ in 3D from 2D, it does prevent the estimate of a 3D spectrum from the 2D results based on assuming the cylindrical symmetry of the interaction.

A typical proton energy spectrum obtained in our 2D PIC simulations for a 50λ spot size, 0.01λ pre-plasma scale length, and 35 fs laser pulse duration is shown in Fig. 7. The proton spectrum is a typical TNSA spectrum, which is exponentially decaying with a sharp cutoff near the maximum energy.

We already showed above that the sweeping regime is more effective in accelerating protons than the one employing small focal diameter laser pulses with the same peak intensity. However, if we compare the number of accelerated protons with the energy higher than half of the cutoff energy, we find that the increase is mostly due to the increase in the focal area. Such a large number of moderately accelerated protons, 4 to 10 MeV, might be especially beneficial to warm-dense matter research.[49]

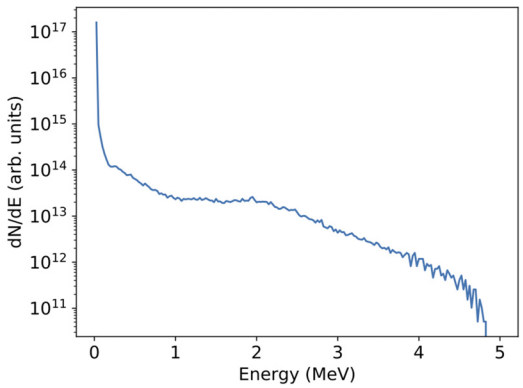

FIG. 7. Typical proton energy spectrum from our simulations.

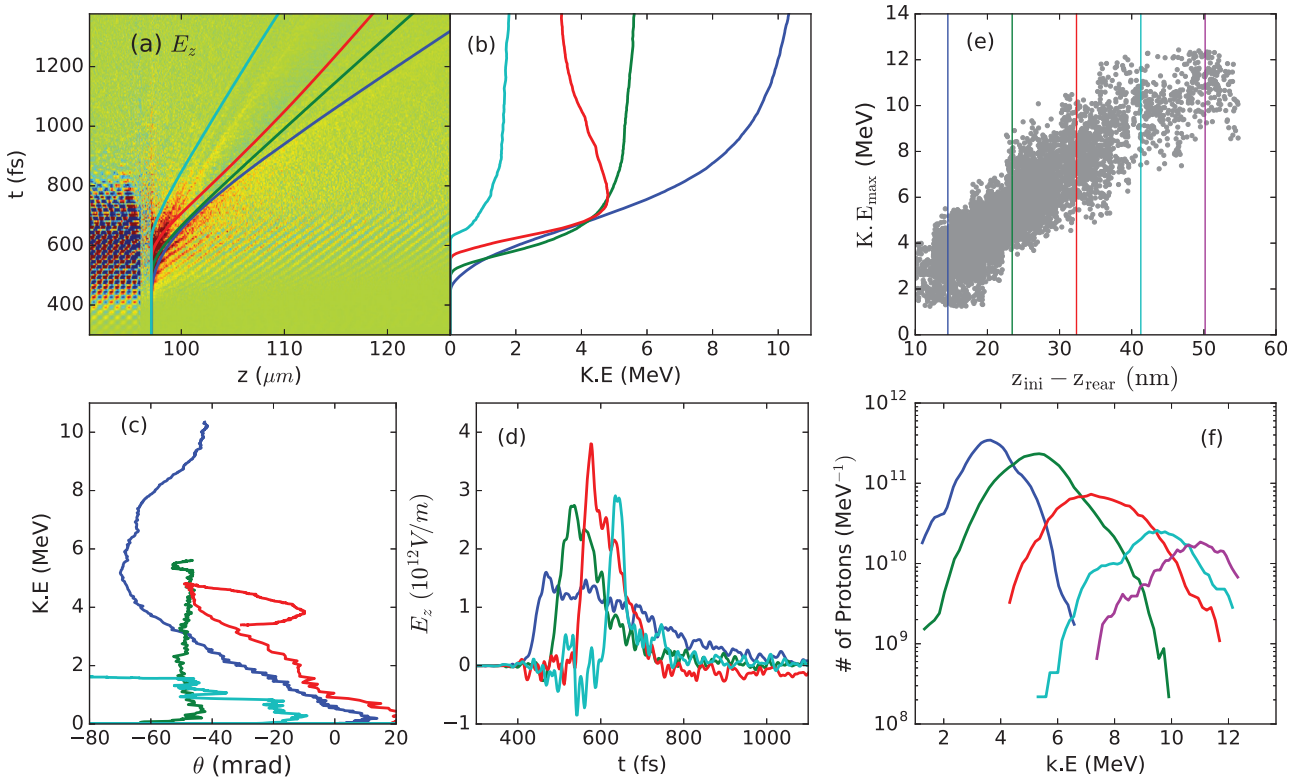

FIG. 8. Individual proton tracking (Run II-4): (a) time evolution of the $E_z(x = 0, z, t)$ field and selected proton trajectories in the $t - z$ space; different colors represent different proton trajectories. (b) and (c) The same proton trajectories in the time-energy space and the energy-angular space. (d) E_z field evolution acting on each proton. The behavior of different parts of proton population depending on the initial position: (e) relationship between the maximum proton energy and the initial distance from the rear surface of the target. Note that z_{rear} marks initial rear boundary of the Ti +11 layer (main target). The protons originate from the pre-formed plasma with exponential distribution. (f) Proton energy spectrum from each sector in (e).

The proton acceleration and the broadness of the energy spectrum are examined further using individual proton tracking, Figs. 8(a)–8(d), and the behavior of the different parts of proton population, chosen based on the initial position in the pre-formed plasma, Figs. 8(e) and 8(f). The evolution of the longitudinal electric field at the central axis, $E_z(x = 0, z, t > 0)$, and individual proton trajectories in the $t - z$ space are shown in Fig. 8(a); different colors represent different proton trajectories. The same proton trajectories are plotted in the $t -$ energy space in Fig. 8(b). A high energy proton, initially farthest from the target back, (blue line) is accelerated by the leading electric field, while relatively low energy protons (red and cyan lines) are accelerated by the trailing electric field. Figure 8(c) shows the angle vs energy curves of the same protons. The protons are tilted toward $\theta < 0$ with an angle around $\theta = -20$ to –50 mrad due to the obliquely propagating laser beam. The evolution of the longitudinal electric field acting on each proton is shown in Fig. 8(d). Interestingly, a high energy proton (blue line) is accelerated by a lower electric field strength for a longer time, while a relatively low energy proton (red or cyan line) is accelerated by a higher electric field strength for a shorter time. That is because high energy protons follow the leading electric field but low energy protons are passed over by the trailing electric field.

The relationship between the maximum proton energy and the initial distance from the rear surface of the target is shown in Fig. 8(e). Here, the protons are selected in the region of $-20 < x(\mu\text{m}) < 20$ and the rear surface at $t = 0$. As the protons are located farther from the surface, they gain higher energy eventually. Figure 8(f) shows the proton energy spectrum in each sector around the line in Fig. 8(e). The broadness of the energy spectrum results from the summation of the energy spectra in different sectors.

We examined the proton beam profile for a large laser focal diameter and found that the proton beam is highly collimated with a small angular divergence.

IV. SUMMARY AND CONCLUSION

We explored proton acceleration based on the TNSA mechanism with an oblique angle of laser incidence and a large focal diameter using a series of 2D particle-in-cell simulations. We found that the ponderomotive scaling dominates for large pre-plasma density gradient scale-lengths ($>0.1\lambda$). However, as the scale length decreases to less than 0.01λ, the electron heating begins to deviate from the ponderomotive scaling, when we vary the laser pulse duration from hundreds of femtoseconds to tens of femtoseconds while keeping the laser total energy constant. It was determined that this effect is due to the laser "sweeping." This sweeping occurs when the laser pulse with a large focal diameter and relatively short duration ($c\tau \leq w_0$) obliquely interacts with a solid density target. In this case, the laser effectively

irradiates only a part of the focal area on the foil, thus reducing the hot electron temperature. As the hot temperature also reduces for a long pulse duration due to the decrease in peak laser intensity, there should be an optimal pulse duration, which maximizes the hot electron temperature. From the geometrical considerations, one can conclude that this duration is $c\tau \sim w_0$, which we confirmed in 2D PIC simulations. It corresponds to the laser pulse irradiating almost all the focal area at the foil while still maintaining rather high peak intensity.

With large focal diameters, the protons reveal a highly achromatic and low angular divergence (50–100 mrad) beam. This is connected with a quasi-one-dimensional geometry of sheath fields at the back of the target. From the particle tracking method, we determined that high energy protons are accelerated by the sheath field, which is due to the expanding proton layer, whereas the bulk of the low to middle energy protons comes from the expanding carbon layer. We found that the final proton energy depends on their initial position in the contamination layer, meaning that the protons located farther from the rear surface of the target got higher energies.

Thus, we explored the deviation of the proton acceleration from TNSA scaling in the case of a large focal diameter laser pulse obliquely incident at a solid density foil. We found that this particular deviation is due to the geometry of interaction, the so-called sweeping effect, and is very sensitive to the pre-plasma density gradient scale length.

ACKNOWLEDGMENTS

We would like to thank Rémi Lehe and Axel Huebl for fruitful discussions. J. H. Bin acknowledges financial support from the Alexander von Humboldt Foundation. This work was supported by LDRD funding from LBNL provided by the Director, and the U.S. DOE Office of Science Offices of HEP and FES (through LaserNetUS), under Contract No. DE-AC02-05CH11231. This research used computational resources (Cori) of the National Energy Research Scientific Computing center (NERSC), which is supported by the Office of Science of the U.S. DOE under Contract No. DE-AC02-05CH11231. This research was supported in part by the Exascale Computing Project (ECP), Project No. 17-SC-20-SC, a collaborative effort of two DOE organizations—the Office of Science and the National Nuclear Security Administration—responsible for the planning and preparation of a capable exascale ecosystem—including software, applications, hardware, advanced system engineering, and early testbed platforms—to support the nation's exascale computing imperative.

APPENDIX: SUMMARY OF THE PERFORMED SIMULATION RUNS

In what follows, we summarize the simulations performed. Table I shows the parameter sets of the 2D TNSA simulations and some output values. Each group contains different pulse durations from $\tau = 35$ to 300 fs. The gradient scale length in the preformed plasma varies from $L = 0$ to 0.1λ in groups I–IV. For comparison with group II, we set a normal laser incidence in group V and a small focal diameter in group VI. Each group has varying laser intensities depending on the pulse duration in order to keep the same laser energy per area. The laser energy absorption to the target, the hot electron temperature, and the acceleration duration of energetic protons are listed.

TABLE I. TNSA simulation parameters and some output values. a_0: dimensionless vector potential, τ: pulse duration, θ_L: angle of laser incidence, w_0: laser waist, L: gradient scale length in the preformed plasma, f_{abs}: laser energy absorption (%) into the target, T_{hot}: hot electron temperature (MeV) during acceleration stage, and τ_{acc}: acceleration time (fs) of high energy protons.

Run	a_0	τ (fs)	$\theta_L(\circ)$	$w_0(\lambda)$	$L(\lambda)$	f_{abs}	T_{hot}	τ_{acc}
I-1	3.30	35	45	50	0	12	0.14	104
I-2	2.11	85	45	50	0	27	0.26	269
I-3	1.86	110	45	50	0	33	0.27	366
I-4	1.66	140	45	50	0	37	0.27	448
I-5	1.35	210	45	50	0	40	0.21	614
I-6	1.13	300	45	50	0	40	0.15	671
II-1	3.30	35	45	50	0.01	24	0.40	102
II-2	2.10	85	45	50	0.01	46	0.52	347
II-3	1.86	110	45	50	0.01	41	0.48	453
II-4	1.66	140	45	50	0.01	53	0.40	516
II-5	1.35	210	45	50	0.01	49	0.27	690
II-6	1.13	300	45	50	0.01	49	0.20	712
III-1	3.30	35	45	50	0.05	34	0.66	89
III-2	2.11	85	45	50	0.05	49	0.63	320
III-3	1.86	110	45	50	0.05	51	0.53	435
III-4	1.66	140	45	50	0.05	49	0.43	483
III-5	1.13	300	45	50	0.05	47	0.23	722
IV-1	3.30	35	45	50	0.1	36	1.03	96
IV-2	2.11	85	45	50	0.1	50	0.74	284
IV-3	1.86	110	45	50	0.1	51	0.60	384
IV-4	1.66	140	45	50	0.1	50	0.49	468
IV-5	1.13	300	45	50	0.1	47	0.26	691
V-1	3.30	35	0	50	0.01	1	0.04	127
V-2	2.11	85	0	50	0.01	4	0.07	208
V-3	1.66	140	0	50	0.01	6	0.09	390
V-5	1.13	300	0	50	0.01	6	0.10	762
VI-1	3.30	35	45	3	0.01	23	0.33	79
VI-2	2.11	85	45	3	0.01	38	0.35	240
VI-3	1.66	140	45	3	0.01	51	0.32	371
VI-4	1.35	210	45	3	0.01	58	0.22	572
VI-5	1.13	300	45	3	0.01	56	0.15	505

DATA AVAILABILITY

The data that support the findings of this study are available from the corresponding author upon reasonable request.

REFERENCES

[1]G. Mourou, T. Tajima, and S. V. Bulanov, Rev. Mod. Phys. **78**, 309 (2006).
[2]H. Daido, M. Nishiuchi, and A. S. Pirozhkov, Rep. Prog. Phys. **75**, 056401 (2012).
[3]A. Macchi, M. Borghesi, and M. Passoni, Rev. Mod. Phys. **85**, 751 (2013).
[4]S. V. Bulanov, J. J. Wilkens, T. Z. Esirkepov, G. Korn, G. Kraft, S. Kraft, M. Molls, and V. S. Khoroshkov, Phys. Usp. **57**, 1149 (2014).
[5]M. Roth and M. Schollmeier, CERN Yellow Rep. **1**, 231 (2016).
[6]S. S. Bulanov, E. Esarey, C. B. Schroeder, S. V. Bulanov, T. Z. Esirkepov, M. Kando, F. Pegoraro, and W. P. Leemans, Phys. Plasmas **23**, 056703 (2016).
[7]E. L. Clark, K. Krushelnick, J. R. Davies, M. Zepf, M. Tatarakis, F. N. Beg, A. Machacek, P. A. Norreys, M. I. K. Santala, I. Watts, and A. E. Dangor, Phys. Rev. Lett. **84**, 670 (2000).

[8]R. A. Snavely, M. H. Key, S. P. Hatchett, T. E. Cowan, M. Roth, T. W. Phillips, M. A. Stoyer, E. A. Henry, T. C. Sangster, M. S. Singh, S. C. Wilks, A. MacKinnon, A. Offenberger, D. M. Pennington, K. Yasuike, A. B. Langdon, B. F. Lasinski, J. Johnson, M. D. Perry, and E. M. Campbell, Phys. Rev. Lett. **85**, 2945 (2000).
[9]A. Maksimchuk, S. Gu, K. Flippo, D. Umstadter, and V. Y. Bychenkov, Phys. Rev. Lett. **84**, 4108 (2000).
[10]S. C. Wilks, A. B. Langdon, T. E. Cowan, M. Roth, M. Singh, S. Hatchett, M. H. Key, D. Pennington, A. MacKinnon, and R. A. Snavely, Phys. Plasmas **8**, 542 (2001).
[11]T. Esirkepov, M. Borghesi, S. V. Bulanov, G. Mourou, and T. Tajima, Phys. Rev. Lett. **92**, 175003 (2004).
[12]A. Henig, S. Steinke, M. Schnurer, T. Sokollik, 3R. Horlein, D. Kiefer, D. Jung, J. Schreiber, B. M. Hegelich, X. Q. Yan, J. Meyer-ter-Vehn, T. Tajima, P. V. Nickles, W. Sandner, and D. Habs, Phys. Rev. Lett. **103**, 245003 (2009).
[13]J. H. Bin, W. J. Ma, H. Y. Wang, M. J. V. Streeter, C. Kreuzer, D. Kiefer, M. Yeung, S. Cousens, P. S. Foster, B. Dromey, X. Q. Yan, R. Ramis, J. Meyer-ter-Vehn, M. Zepf, and J. Schreiber, Phys. Rev. Lett. **115**, 064801 (2015).
[14]D. Haberberger, S. Tochitsky, F. Fiuza, C. Gong, R. A. Fonseca, L. O. Silva, W. B. Mori, and C. Joshi, Nat. Phys. **8**, 95 (2012).
[15]S. Palaniyappan, B. M. Hegelich, H.-C. Wu, D. Jung, D. C. Gautier, L. Yin, B. J. Albright, R. P. Johnson, T. Shimada, S. Letzring, D. T. Offermann, J. Ren, C. Huang, R. Horlein, B. Dromey, J. C. Fernandez, and R. C. Shah, Nat. Phys. **8**, 763 (2012).
[16]A. V. Kuznetsov, T. Zh. Esirkepov, F. F. Kamenets, and S. V. Bulanov, Plasma Phys. Rep. **27**, 211 (2001); S. V. Bulanov and T. Zh. Esirkepov, Phys. Rev. Lett. **98**, 049503 (2007).
[17]S. S. Bulanov, E. Esarey, C. B. Schroeder, W. P. Leemans, S. V. Bulanov, D. Margarone, G. Korn, and T. Haberer, Phys. Rev. Spec. Top.-Accel. Beams **18**, 061302 (2015).
[18]F. Wagner, O. Deppert, C. Brabetz, P. Fiala, A. KleinSchmidt, P. Poth, V. A. Schanz, A. Tebartz, B. Zielbauer, M. Roth *et al.*, Phys. Rev. Lett. **116**, 205002 324 (2016).
[19]J. P. Freidberg, R. W. Mitchell, R. L. Morse, and L. I. Rudsinski, Phys. Rev. Lett. **28**, 795 (1972).
[20]W. L. Kruer and K. Estabrook, Phys. Fluids **28**, 430 (1985).
[21]F. Brunel, Phys. Rev. Lett. **59**, 52 (1987).
[22]L. Robson, P. T. Simpson, R. J. Clarke, K. W. D. Ledingham, F. Lindau, O. Lundh, T. McCanny, P. Mora, D. Neely, C.-G. Wahlström *et al.*, Nat. Phys. **3**, 58 (2007).
[23]H. Schwoerer, S. Pfotenhauer, O. Jäckel, K.-U. Amthor, B. Liesfeld, W. Ziegler, R. Sauerbrey, K. W. D. Ledingham, and T. Esirkepov, Nature **439**, 445 (2006).
[24]M. Borghesi, Nucl. Inst. Methods Phys. Res., Sect. A **740**, 6 (2014).
[25]P. Gibbon and E. Förster, Plasma Phys. Controlled Fusion **38**, 769 (1996).
[26]S. C. Wilks and W. L. Kruer, IEEE J. Quantum Electron. **33**, 1954 (1997).
[27]A. J. Mackinnon, M. Borghesi, S. Hatchett, M. H. Key, P. K. Patel, H. Campbell, A. Schiavi, R. Snavely, S. C. Wilks, and O. Willi, Phys. Rev. Lett. **86**, 1769 (2001).
[28]Y. Sentoku, V. Y. Bychenkov, K. Flippo, A. Maksimchuk, K. Mima, G. Mourou, Z. M. Sheng, and D. Umstadter, Appl. Phys. B **74**, 207 (2002).
[29]P. Mora, Phys. Rev. Lett. **90**, 185002 (2003).
[30]Y. Oishi, T. Nayuki, T. Fujii, Y. Takizawa, X. Wang, T. Yamazaki, K. Nemoto, T. Kayoiji, T. Sekiya, K. Horioka, Y. Okano, Y. Hironaka, K. G. Nakamura, K. Kondo, and A. A. Andreev, Phys. Plasmas **12**, 073102 (2005).
[31]E. d'Humieres, E. Lefebvre, L. Gremillet, and V. Malka, Phys. Plasmas **12**, 062704 (2005).
[32]A. A. Andreev, R. Sonobe, S. Kawata, S. Miyazaki, K. Sakai, K. Miyauchi, T. Kikuchi, K. Platonov, and K. Nemoto, Plasma Phys. Controlled Fusion **48**, 1605 (2006).
[33]J. Fuchs, C. A. Cecchetti, M. Borghesi, T. Grismayer, E. d'Humières, P. Antici, S. Atzeni, P. Mora, A. Pipahl, L. Romagnani, A. Schiavi, Y. Sentoku, T. Toncian, P. Audebert, and O. Willi, Phys. Rev. Lett. **99**, 015002 (2007).
[34]R. Nuter, L. Gremillet, P. Combis, M. Drouin, E. Lefebvre, A. Flacco, and V. Malka, J. Appl. Phys. **104**, 103307 (2008).
[35]M. Carrie, E. Lefebvre, A. Flacco, and V. Malka, Phys. Plasmas **16**, 053105 (2009).
[36]S. Steinke, J. H. Bin, J. Park, Q. Ji, K. Nakamura, A. J. Gonsalves, S. S. Bulanov, C. Toth, J.-L. Vay, C. B. Schroeder, E. Esarey, T. Schenkel, and W. P. Leemans, Phys. Rev. AB **23**, 021302 (2020).
[37]J.-L. Vay, D. P. Grote, R. H. Cohen, and A. Friedman, Comput. Sci. Discovery **5**, 014019 (2012).
[38]See http://blast.lbl.gov/blast-codes-warp/ for the description of the PIC code WARP.
[39]H. Abe, N. Sakairi, R. Itatani, and H. Okuda, J. Comp. Phys. **63**, 247 (1986).
[40]P. Mckenna, D. C. Caroll, 1O. Lundh, F. Nurnberg, K. Markey, S. Bandyopadhyay, D. Batani, R. G. Evans, R. Jafer, S. Kar, D. Neely, D. Pepler, M. N. Quinn, R. Redaelli, M. Roth, C.-G. Wahlstrom, X. H. Yuan, and M. Zepf, Laser Part. Beams **26**, 591 (2008).
[41]W. P. Wang, B. F. Shen, H. Zhang, Y. Xu, Y. Y. Li, X. M. Lu, C. Wang, Y. Q. Liu, J. X. Lu, Y. Shi, Y. X. Leng, X. Y. Liang, R. X. Li, N. Y. Wang, and Z. Z. Xu, Appl. Phys. Lett. **102**, 224101 (2013).
[42]T. Z. Esirkepov, J. K. Koga, A. Sunahara, T. Morita, M. Nishikino, K. Kageyama, H. Nagatomo, K. Nishihara, A. Sagisaka, H. Kotaki, T. Nakamura, Y. Fukuda, H. Okada, A. S. Pirozhkov, A. Yogo, M. Nishiuchi, H. Kiriyama, K. Kondo, M. Kando, and S. V. Bulanov, Nucl. Instrum. Methods Phys. Res., Sect. A **745**, 150 (2014).
[43]P. Hadjisolomou, I. P. Tsygvintsev, P. Sasorov, V. Gasilov, G. Korn, and S. V. Bulanov, Phys. Plasmas **27**, 013107 (2020).
[44]V. S. Popov, Phys.-Usp. **47**, 855 (2004).
[45]J. May, J. Tonge, I. Ellis, W. B. Mori, F. Fiuza, R. A. Fonseca, L. O. Silva, and C. Ren, Phys. Plasmas **21**, 052703 (2014).
[46]S. C. Wilks, W. L. Kruer, M. Tabak, and A. B. Langdon, Phys. Rev. Lett. **69**, 1383 (1992).
[47]A. Flacco, F. Sylla, M. Veltcheva, M. Carrié, R. Nuter, E. Lefebvre, D. Batani, and V. Malka, Phys. Rev. E **81**, 036405 (2010).
[48]P. Gibbon and A. R. Bell, Phys. Rev. Lett. **68**, 1535 (1992).
[49]M. Roth, I. Alber, V. Bagnoud, C. R. D. Brown, R. Clarke, H. Daido, J. Fernandez, K. Flippo, S. Gaillard, C. Gauthier, M. Geissel, S. Glenzer, G. Gregori, M. Günther, K. Harres, R. Heathcote, A. Kritcher, N. Kugland, S. LePape, B. Li, M. Makita, J. Mithen, C. Niemann, F. Nurnberg, D. Offermann, A. Otten, A. Pelka, D. Riley, G. Schaumann, M. Schollmeier, J. Schuttrumpf, M. Tampo, A. Tauschwitz, and A. Tauschwitz, Plasma Phys. Controlled Fusion **51**, 124039 (2009).